Iranian Journal of Science and Technology, Transactions of Civil Engineering (2023) 47:2799–2814
https://doi.org/10.1007/s40996-023-01083-0

RESEARCH PAPER

Nonlinear Behaviors of Ultra-High-Performance Concrete-Filled Steel Tubular Beam-Column Under Monotonic and Cyclic Loading

Heng Cai[1,2] · Chujun Li[1] · Fangqian Deng[2]

Received: 18 October 2022 / Accepted: 25 February 2023 / Published online: 15 March 2023

Abstract
In this work, a novel fiber beam element (FBE) model was established to predict the nonlinear behaviors of ultra-high-performance concrete-filled steel tubular members (UHPCFSTs) considering local buckling of steel tubes and passive confinement effect. The validity of the FBE model under different loading conditions (monotonic and cyclic loading) was thoroughly verified using comprehensive published data. Meanwhile, an experimental database of rectangular UHPCFST members subjected to combined axial compression and flexure was established with ξ ranging from 0.375 to 3.011. The suitability of the current code provisions for predicting the ultimate bending strengths was evaluated using the experimental database. Finally, a novel and simplified *N–M* interaction curve was constructed to predict the ultimate bending strengths of UHPCFSTs. The results indicated that ignoring local buckling of steel tubes would overestimate peak strengths and post-peak ductility of UHPCFSTs by up to 16.4%. Obviously, this is adverse for structural design. When the width-to-thickness ratios were reduced to less than 30, the local buckling could be neglected. Compared with experimental results, the ultimate bending strengths of UHPCFSTs were undervalued by the current code provisions such as AISC360-10, AIJ, GB50936 and EC4 with computed mean values (MVs) of 0.833, 0.863, 0.799 and 0.869, respectively. Experimental and predicted results showed good agreement with a MV of 1.04.

Keywords UHPCFST · Fiber beam element model · Experimental database · Local buckling · Ultimate bending strength

Abbreviations

f_c	Compressive strength of UHPC
A_c	Area of UHPC
ξ	Confinement index
ε_{cc}	Peak strain of confined UHPC
α, ζ, r	Parameters
f_{cy}	Plateau stress
ε_y	Yield strain of steel
E_s	Elastic modulus of steel
b, h, t	Width, height and thickness
N_{ue},N_{uc}	Tested, computed axial peak loads
P_{ue}, P_{uc}	Tested, computed lateral peak loads
L	Length of column
M_u	Pure bending strength
γ_m	Plastic coefficient
f_{sc}	Composite strength
α_s	Steel ratio
f_y	Yield strength of steel
A_s	Area of steel tube
ε_c	Peak strain of UHPC without confinement
f_{cc}	Peak strength of confined UHPC
e_c	Elastic modulus of UHPC
f_{el}	Effective confined pressure
w_s	Coefficient of width-to-thickness ratio
φ	Curvature
e_0	Eccentric distance
Δ	Deflection
n	Axial compression ratio
M_t, M_c	Computed, tested ultimate bending strength
N_{ut}	Tensile load
W_{sc}	Flexural modulus
f_t	Tensile strength of UHPC
N_0	Imposed axial compression load

✉ Heng Cai
caiheng0311@whu.edu.cn

[1] School of Civil Engineering, Hubei Polytechnic University, Huangshi 435003, China

[2] School of Civil Engineering, Wuhan University, Wuhan 430072, China

1 Introduction

As a future-oriented cement-based material, ultra-high-performance concrete (UHPC) offers ultra-high strength, high toughness and favorable durability (Zohrevand and Mirmiran 2011; Hassan et al. 2012; Hannawi et al. 2016; Xu et al. 2019a). However, UHPC without confinement exhibits high brittleness under compression, limiting its wide application in engineering construction. To overcome this drawback, UHPC is poured into steel tubes (or fiber reinforce plastic tube) to improve ductility (Xu et al. 2019b; Cai et al. 2021). Along with superior mechanical behaviors, the formed UHPC-filled steel tube members (UHPCFSTs) show several advantages over concrete-filled steel tube members (CFSTs) in reducing self-weight, amount of cement and carbon emissions. As a new type of high-performance composite structure, UHPCFSTs have a broad application prospect in modern structures including super high-rise buildings, long-span bridges and heavy haul railway. Currently, many experimental studies have focused on the nonlinear responses of rectangular UHPCFST members such as axial compression behavior (Chen et al. 2018; Yan et al. 2019), eccentric compression behavior (Zhang et al. 2020; Yan et al. 2021a, b) and flexure behavior (Guler et al. 2012; Huang et al. 2020; Li et al 2021). These achievements lay the foundation for the applications of UHPCFSTs.

Several numerical methods have been put forward to predict nonlinear responses of CFSTs such as three dimensional (3D) finite element method and fiber beam element (FBE) model (Han 2016). In addition, differential quadrature and Bezier methods (Kabir and Aghdam 2019; Yan et al. 2021a) were also alternatively used to predict nonlinear behaviors of CFST beam-column under axial compression due to their high stability and accuracy. FBE model exhibits higher efficiency than 3D finite element model in computing nonlinear behaviors of complex structures. At present, the FBE model is widely used to compute static (Vrcelj and Uy 2002; Ahmed et al. 2012, 2020), seismic (Valipour and Foster 2010; Jiang et al. 2019), fire resistance (Kamila et al. 2019) and impact-resistance behaviors of CFSTs. The accuracy of FBE model is largely dependent on the input materials and interactions between the steel tube and concrete such as confinement effect, local buckling of steel tubes and bond-slip in the interface.

Studies have shown that steel tubes under compression, especially those with square and rectangular steel shape with large width-to-thickness ratios, are liable to be locally buckled due to the initial defect (as shown in Fig. 1). This is attributed to the unequal stress distribution in rectangular steel tubes and smaller critical buckling stress due to the larger width-to-thickness ratio. Local buckling significantly affects the static and cyclic behaviors of thin-walled CFSTs (Valipour and Foster 2010; Liang et al. 2007; Cai et al. 2022). Generally, two methods are adopted when considering the local buckling in FBE model. The first one is using effective distribution width (Uy 2000; Vrcelj and Uy 2002; Ahmed et al. 2012, 2020), whereby steel tubes in ineffective distribution width are out of work due to local buckling and the longitudinal stress is zero. However, it is difficult to determine the critical buckling stress and effective distribution width is difficult because the regression analysis for different types of steel shows a significant deviation, resulting in computational problem.

Similar to this work, several studies also considered local buckling by modifying envelopes of steel. However, such studies focused on the static behaviors of CFSTs under monotonic loading (Lai and Varma 2016; Lai et al. 2016; Tao et al. 2021) with concrete strength no more than 90 MPa. Because of the lack of rectangular steel tube-confined UHPC model, few studies have investigated nonlinear behaviors of UHPCFSTs using the FBE model. Besides, the current code provisions were mainly formulated based on results on CFSTs. Considering the difference in mechanical properties between UHPC and ordinary concrete, whether

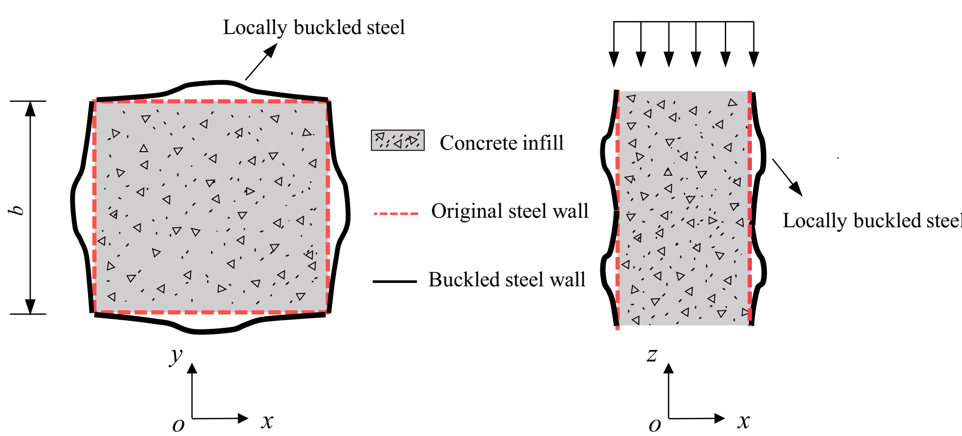

Fig. 1 Local buckling of steel tubes

these code provisions are suitable for UHPCFTSTs needs to be further researched.

In this paper, the effective compressive envelopes of steel and confined UHPC model were successfully incorporated into the FBE model to consider the local buckling and passive confinement effect on the UHPC. Meanwhile, an experimental database of UHPCFST members was established, which covered a wide range of material and geometric parameters. Using this database, the nonlinear static and cyclic behaviors of UHPCFTs were computed to verify the validity of the FBE model, the effects of local buckling on the performance of UHPCFSTs were evaluated, and the suitability of current code provisions were comprehensively evaluated. Finally, a novel and simplified *N*–*M* interaction curve was established to predict the ultimate bending strength of UHPCFSTs.

2 Modeling Technology

The FBE model (Han 2016) was performed on MATLAB, as shown in Fig. 2, the element was meshed as 0.5 mm for each fiber. The bond-slip in the interface was neglected.

2.1 Stress–Strain Model of UHPC and Steel

2.1.1 UHPC

As discussed previously, the accuracy of FBE model is largely dependent on the input materials and interaction between the steel tubes and concrete. The strength and ductility of concrete can be improved through confinement by steel tubes. Therefore, passive confinement effect should be considered in FBE model. The current stress–strain models of confined UHPC (Le and Fehling 2017; Le et al. 2018; Ren et al. 2017) are mainly focused on circle steel tubes.

For rectangular steel tubes, the confined stress is non-uniform. A stress–strain model of rectangular steel tube-confined UHPC based on equivalent method was proposed in our previous work (Cai et al. 2022), which included two branches:

The ascending branch

$$\sigma_{\mathrm{c}} = f_{\mathrm{cc}}\left[\frac{r(\varepsilon/\varepsilon_{\mathrm{cc}})}{r-1+(\varepsilon/\varepsilon_{\mathrm{cc}})^{r}}\right], r = \frac{E_{\mathrm{c}}}{E_{\mathrm{c}} - f_{\mathrm{cc}}/\varepsilon_{\mathrm{cc}}},\ \varepsilon \le \varepsilon_{\mathrm{cc}} \tag{1}$$

The descending and horizontal branches

$$\sigma_{\mathrm{c}} = f_{\mathrm{cy}} + (f_{\mathrm{cc}} - f_{\mathrm{cy}})\exp\left[-\left(\frac{\varepsilon-\varepsilon_{\mathrm{cc}}}{\alpha}\right)^{\varsigma}\right],\ f_{\mathrm{cy}}=0.81f_{\mathrm{cc}} - 48,\ \varepsilon > \varepsilon_{\mathrm{cc}} \tag{2}$$

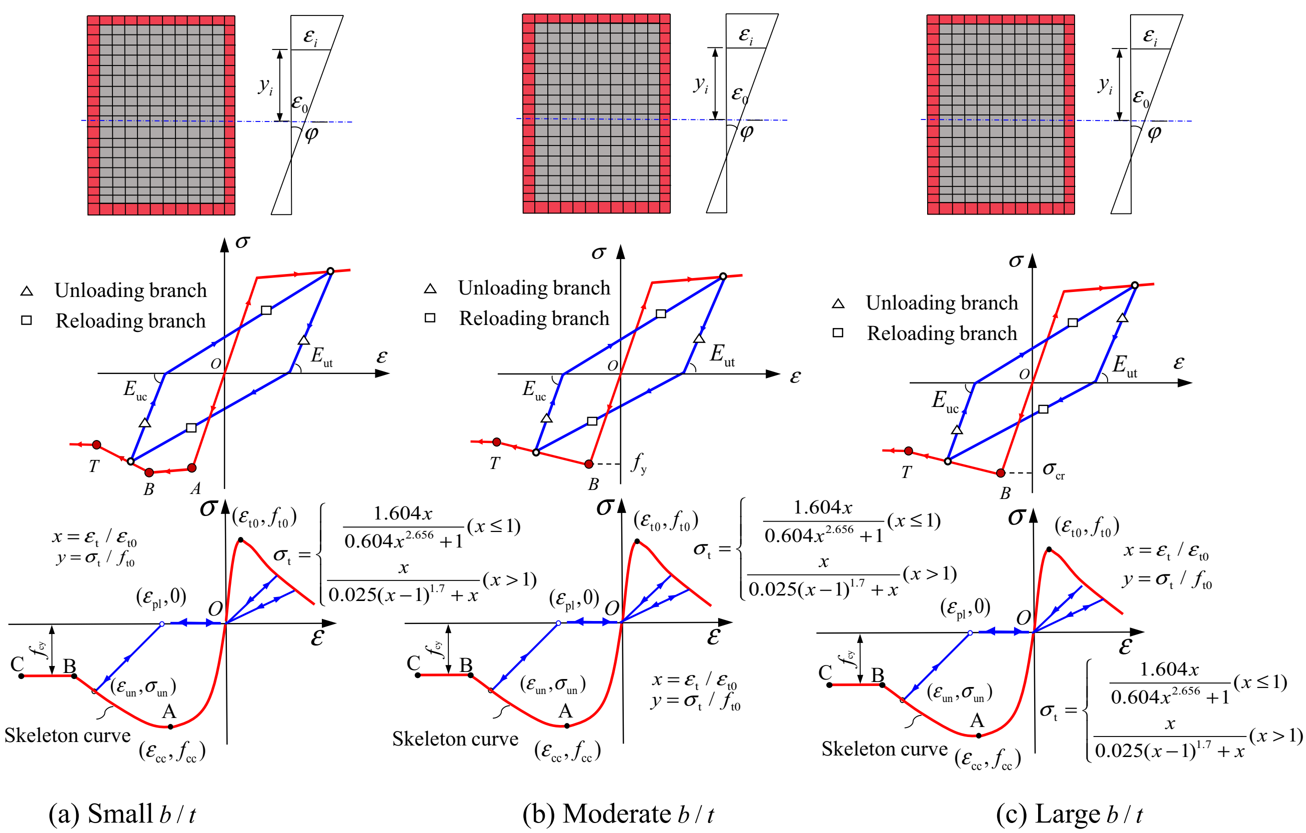

Fig. 2 The FBE model of UHPCFSTs

where E_c is the elastic modulus of UHPC which is taken as $3840\sqrt{f_c}$(Graybeal 2007);f_{cy}(Unit: MPa) denotes plateau stress; α and ζ are the parameters determining the shape of the descending branches,ζ is the constant,$\zeta = 4.0$(Cai et al. 2022),$\alpha = 0.005 + 0.0075\xi$,$\xi$ denotes confinement index which is taken as $A_s f_y/(A_c f_c)$, A_s, A_c are the areas of steel tube and UHPC, f_y is the yield strength of steel, f_c is the peak strength of UHPC without confinement; ε_{cc} (Unit: ε) and f_{cc} (Unit: MPa) denote the peak stress and strain considering passive confinement effect, which are given by:

$$\varepsilon_{cc}/\varepsilon_c = 4.67\exp[-24(f_{cc}/f_c - 1)] + 1.57, f_{cc}/f_c = 1 + 0.051\exp(38.3f_{el}/f_c) \quad (3)$$

where f_{el} denotes the effective confined pressure (Cai et al. 2022),ε_c denotes peak strain without confinement, which is given as (Le and Fehling 2017):

$$\varepsilon_c = 0.00083f_c^{0.276} \quad (4)$$

The constitutive model of UHPC under uniaxial tension (Hu et al. 2018) was adopted in this work, as shown in Fig. 2. The residual plastic strain (ε_{pl}) (Mander et al. 1988) was calculated when unloading from compressive envelope curve, whilst the unloading branch pointed to the origin when unloading from tensile envelope curve.

2.1.2 Steel

In this work, a bilinear model with a hardening stiffness of 0.01 E_s (E_s=205 GPa) was adopted for steel under tension, and local buckling was taken into account for compressive envelope curve. Sakino et al. (2004) put forward an effective compressive stress–strain model, in which local buckling was considered by reducing the strength and creating descending branches. The model is divided into three categories according to width-to-thickness ratio, as shown in Fig. 3. The parameters of key points are shown in Table 1.

In this model, stiffness is no longer E_s when unloading from compressive and tensile envelopes. To consider the reduction of stiffness caused by local buckling, the unloading stiffness in compressive envelope curve (E_{uc}) by Dhakal and Maekawa (2002) was adopted, as given in Eq. (5):

$$E_{uc}/E_s = (f_{s,min}/f_{t,min})^2 \quad (5)$$

where $f_{s,min}$ and $f_{t,min}$ denote the stresses at the minimum strain point on the compressive skeleton curve with and without considering local buckling, respectively. Using the method by Dodd and Restrepo-Posada (1995), unloading stiffness (E_{ut}) in tensile envelope curve was calculated, as shown in Eq. (6):

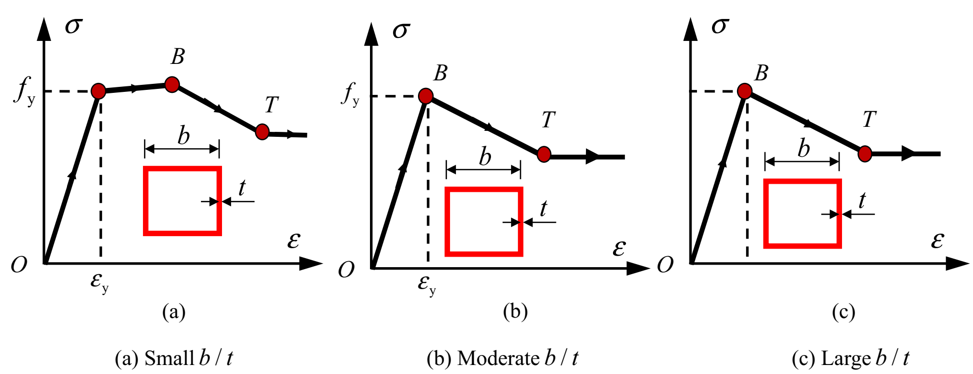

Fig. 3 The compressive envelopes of steel

Table 1 The parameters of effective envelopes of steel (Sakino et al. 2004)

Critical points		$\sqrt{w_s} \le 1.54$	$1.54 < \sqrt{w_s} < 2.03$	$2.03 \le \sqrt{w_s}$
P	σ_P	$f_y/(0.698 + 0.128w_s)$	f_y	$f_y/(0.698 + 0.07w_s)$
	ε_P	$(6.06/w_s^2 - 0.801/w_s + 1.1)\varepsilon_y$	ε_y	σ_B/E_s
S	σ_S	$(1.19 - 0.207\sqrt{w_s})\sigma_B$	$(1.19 - 0.207\sqrt{w_s})\sigma_B$	$(1.19 - 0.207\sqrt{w_s})\sigma_B$
	ε_s	$\varepsilon_B + 3.59\varepsilon_y$	$4.59\varepsilon_y$	$4.59\sigma_B/E_s$

w_s denotes coefficient of b/t, $w_s = (b/t)^2\varepsilon_y$

$$E_{ut}/E_s = 0.82 + \frac{1}{5.55 + 1000\varepsilon_{s,\max}} \quad (6)$$

where $\varepsilon_{s,\max}$ is the maximum plastic tensile strain.

2.2 Computation procedure of FBE Model

The computation steps for the FBE model were as follows:

1. Geometric and physical parameters were inputted into the model.
2. Section was discretized into fibers and the coordinates were obtained.
3. An curvature increment φ and lateral displacement Δ were computed.
4. Assuming the strain at the neutral axis (ε_0), fiber stress σ_{ci} and σ_{si} was calculated according to strains and loading history.
5. Axial force N_{in} and ultimate bending strength M_{in}. were computed.
6. Two loading paths were evaluated to determine whether the equilibrium conditions were satisfied: $|N_{in}-N| < 10^{-2}$, $|M_{in}- N_{in}(e_0 + \Delta_i)|/ M_{in} < 10^{-2}$. If not, steps 4–6 were repeated until the equilibrium condition was satisfied. Then, the lateral force P_i was computed. In this step, the ε_0 was determined by dichotomy.
7. Steps 3–7 were repeated and the data was recorded until the maximum curvature was reached.
8. N–Δ and P–Δ curves were plotted.

A flow diagram of the computation process is shown in Fig. 4.

3 Model Validation

To validate the universality and reliability of the FBE model, experimental results on UHPCFST members in published literature were collected for validation.

3.1 UHPCFST Short Columns Under Axial Compression

The axial compression behavior of UHPCFST short columns with both ends hinged was tested by Chen et al. (2018) and Xiong et al. (2017a) using the axial displacement loading pattern. The material parameters of partial specimens are summarized in Table 2. The axial load-axial strain (N–ε) curves were computed with and without local buckling considered using FBE model, as shown in Figs. 5 and 6.

In Figs. 5 and 6, the axial force exactly reached its peak when the axial stress of UHPC reached f_{cc}. In addition, due to the bond-slip in the interface, certain deviations

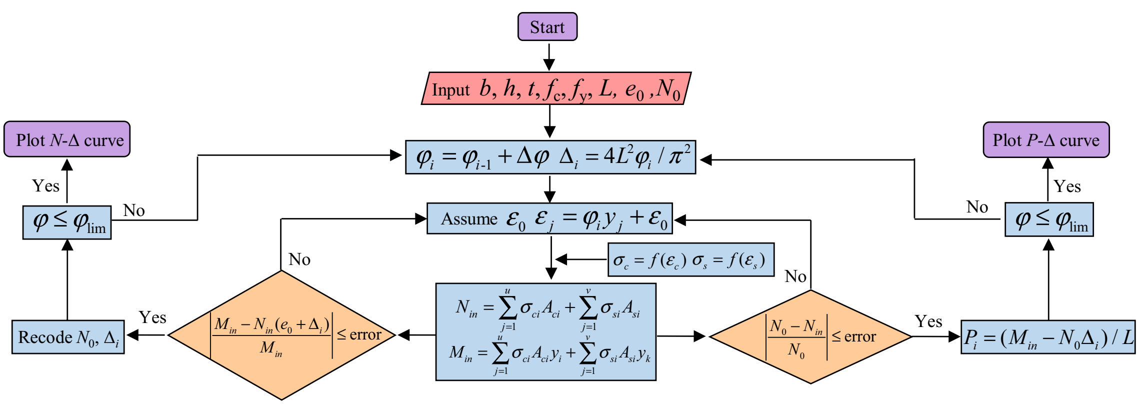

Fig. 4 A flow diagram of the computation process

Table 2 Details of specimen for computation (Chen et al. 2018; Xiong et al. 2017a)

Source	Specimen name	b/t	f_c (MPa)	f_y (MPa)	$\varepsilon_{cc,e\,(\mu\varepsilon)}$	$\varepsilon_{cc,\,c(\mu\varepsilon)}$	N_{ue} (kN)	N_{uc} (kN)	$\|\varepsilon_{cc,e}$-$\varepsilon_{cc,c}\|/\varepsilon_{cc,e}$	$\|N_{ue}$–$N_{uc}\|/N_{ue}$
Chen et al. (2018)	SS1-2	50	113.2	348.7	7600	7010	1406	1394	7.76%	0.85%
	SS1-3	50	130.8	348.7	7022	7510	1575	1578	6.95%	0.19%
Xiong et al. (2017a)	S2	18.8	157.2	779	4711	5010	6715	6998	6.35%	4.21%
	S3	18.8	147	779	5022	5010	6616	6844	0.23%	3.45%

$\varepsilon_{cc,e}$, $\varepsilon_{cc,c}$ are the tested and computed peak strains, N_{ue} and N_{uc} are the tested and computed peak loads

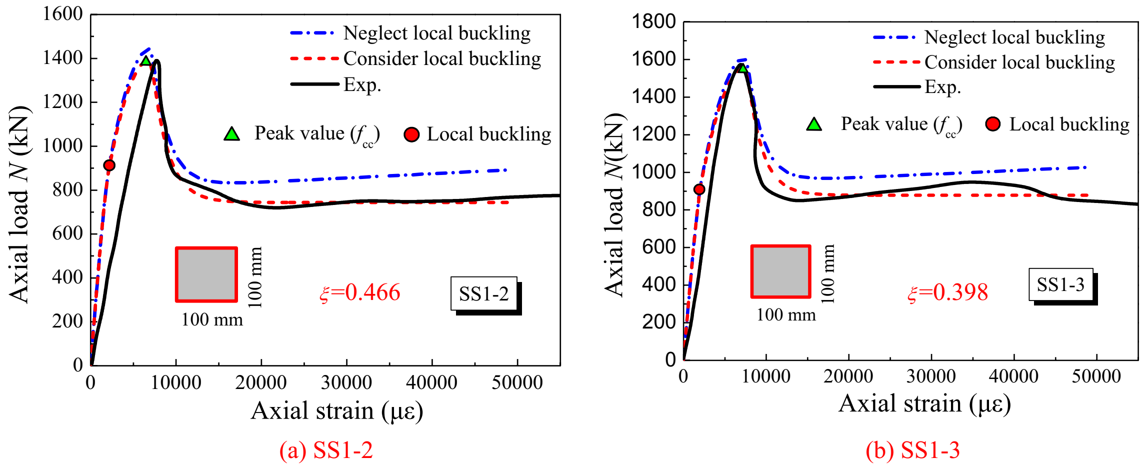

Fig. 5 The computation of N–ε curves (Chen et al. 2018)

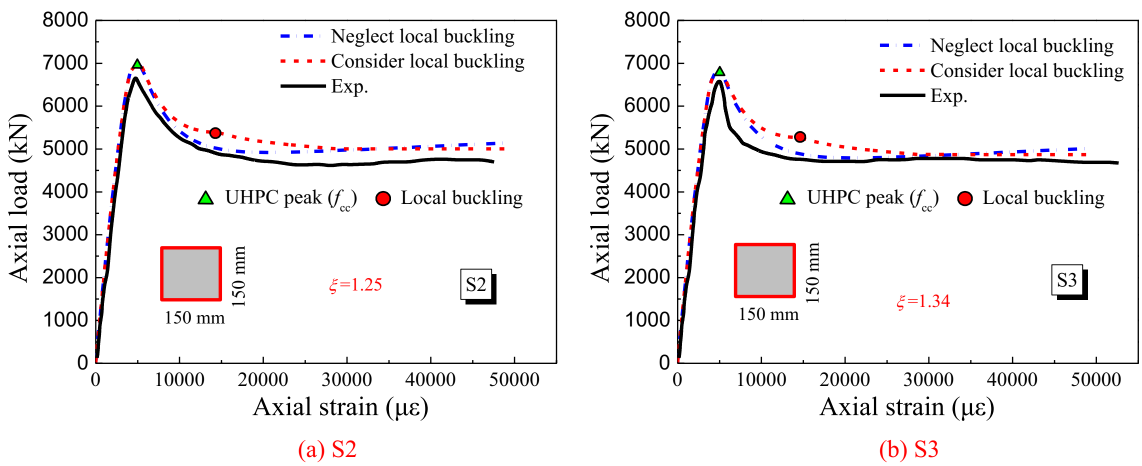

Fig. 6 The computation of N–ε curves (Xiong et al. 2017a)

were observed in the ascending branch between the computation and test results. The failure modes of UHPCFSTs under axial compression were governed by the confinement indexes ξ. For specimens SS1-2 and SS1-3 with small ξ of 0.466 and 0.398, respectively, compression failure occurred on the principal shear plane with crack (Chen et al. 2018). At a higher b/t value, neglecting local buckling for this series overestimated the peak loads and residual strengths. For specimens S2 and S3 with relatively large ξ of 1.25 and 1.34, respectively, the failure with multiple bulges occurred. At lower b/t value, the effect of local buckling was negligible.

Besides, the errors of peak strains and peak loads between the computed results and tested values were within the range of 8%, indicating the correctness and reliability of the FBE

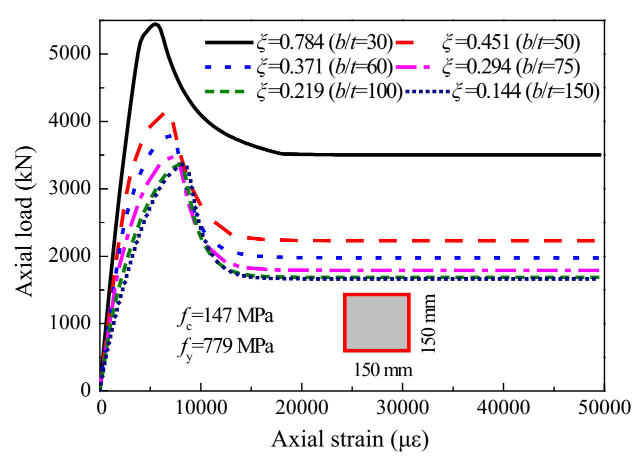

Fig. 7 The effect of confinement index on the N–ε curves

Table 3 Details of specimen for computation (Zhang et al. 2020)

Source	Specimen name	b/t	e_0 (mm)	f_c (MPa)	f_y (MPa)	N_{ue} (kN)	N_{uc} (kN)	$\lvert N_{ue}\text{-}N_{uc}\rvert/N_{ue}$
Zhang et al. (2020)	SS4-S-30	30	30	145.9	430.6	1401	1490	6.35%
	SS4-S-50	30	50	145.9	430.6	1052	1100	4.56%

e_0 is the eccentric distance

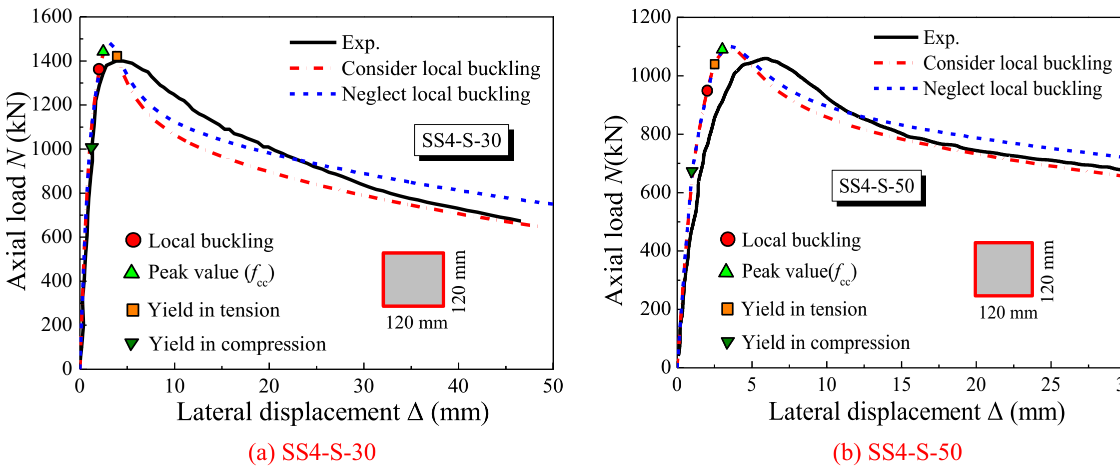

Fig. 8 The computation of N–Δ curves (Zhang et al. 2020)

model. To further analyze the effect of confinement index on the behavior of UHPCFSTs, a parametric analysis was conducted. As can be seen in the analysis result in Fig. 7, the peak load and residual strength increased concomitantly with increasing confinement index, and the specimen exhibited greater stiffness in the ascending branch.

3.2 UHPCFSTs Subjected to Eccentric Compression

The eccentric behavior of square UHPCFST short columns with both ends hinged was tested by Zhang et al. (2020) using the displacement loading pattern. The material parameters of partial specimens are summarized in Table 3. The axial force-lateral displacement (N–Δ) curves were computed with and without local buckling considered using FBE model, as shown in Fig. 8.

Notably, the compressive yield occurred at relatively low load levels because of the small value of strength ratio f_y/f_c, the axial load reached its peak at the point where peak stress (f_{cc}) was slightly exceeded. The in-plane bending failure was observed for this series (Zhang et al. 2020). Similarly, local buckling had little effects on the peak load and post-peak ductility because of the small width-to-thickness ratio ($b/t = 30$), which were negligible.

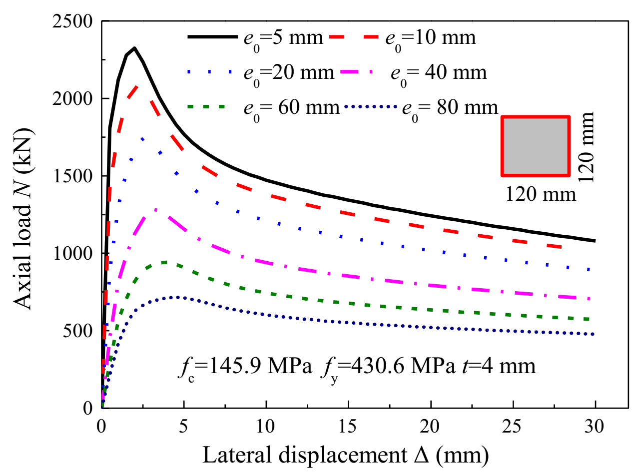

Fig. 9 The effects of eccentric distance on N–Δ curves

The errors of peak loads between the computed results and tested values were within the range of 7%, which further demonstrated the correctness of the FBE model. To further analyze the effect of eccentric distance on the behavior of UHPCFSTs, a parametric analysis was conducted. As can be seen in the analysis result shown in Fig. 9, the peak load and negative stiffness (descending branch) decreased with the increase in eccentric distance.

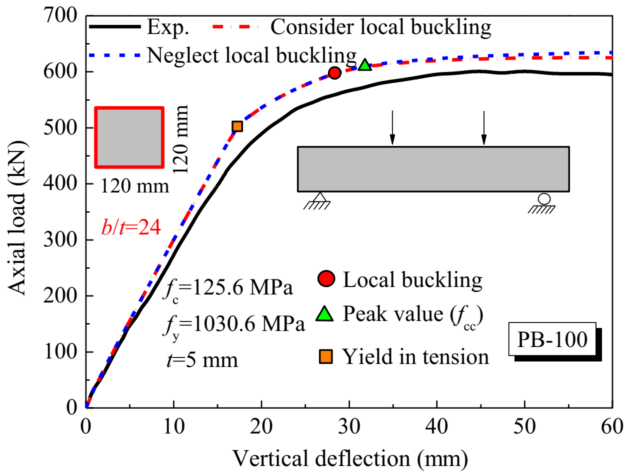

Fig. 10 Computation of F–Δ curves(Huang et al. 2020)

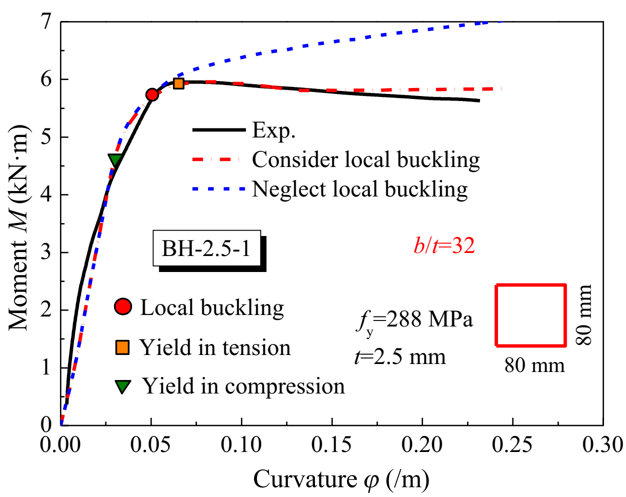

Fig. 11 Computation of M–φ curves (Guler et al. 2012)

3.3 Flexural Behavior of UHPCFSTs

The performance of UHPCFST beams with both ends hinged under flexure was tested by Huang et al. (2020) and Guler et al. (2012) using the displacement loading pattern, with section sizes of 120 mm × 120 mm × 5 mm and 80 mm × 80 mm × 2.5 mm, respectively. In this work, the vertical load–deflection (F–Δ) curve at mid-span and moment–curvature (M–φ) curve were computed and the results are shown in Figs. 10 and 11.

As can be seen in Fig. 10, local buckling occurred at high displacement due to the small b/t (24) and had little effects on the performance of UHPCFST beam under flexure. Further, as shown in Fig. 11, for the hollow steel tube with a small b/t of 32, neglecting local buckling overvalued post-peak ductility. This is mainly because the hollow steel tubes are susceptible to be locally buckled subjected to flexure.

3.4 Cyclic Behavior of UHPCFSTs

The performance of UHPCFST cantilever columns under cyclic loading was tested by Cai (2022) using the displacement loading pattern. Details of partial specimens are summarized in Table 4. The lateral load–displacement (P–Δ) hysteretic curves were computed, and results are as shown in Fig. 12.

The failure modes of UHPCFST columns under cyclic loading were governed by the axial compression ratio (Cai 2022). When the axial compression ratios were 0 and 0.15 (Fig. 12a, b), flexure failure was observed, but the effect of local buckling was insignificant. However, as the axial compression ratio increased to 0.45 (Fig. 12c), the failure modes of UHPCFSTs changed from the flexure failure to compression-flexure. In this case, ignoring local buckling greatly overvalued the peak load and post-peak ductility, with peak load overestimated by 16.4% (the computed and test values were 113.4 kN and 97.4 kN, respectively).

Similarly, for the specimens under small stress levels in Fig. 12d–f, the influence of local buckling tended to increase gradually as b/t increased from 30 to 60.

The errors of peak loads for this series were approximately within the range of 9%.

Table 4 Details of specimen for computation (Cai 2022)

Source	Specimen name	b/t	n	f_c (MPa)	f_y (MPa)	P_{ue} (kN)	P_{uc} (kN)	$\|P_{ue}-P_{uc}\|/P_{ue}$
Cai (2022)	S-3-0-1	50	0	110.3	486	67.5	61.8	8.44%
	S-3-0.15-1	50	0.15	110.3	486	89.3	81.7	8.51%
	S-3-0.45-1	50	0.45	110.3	486	97.4	89.8	7.80%
	S-5-0.15-1	30	0.15	110.3	417	123.6	106.3	14.0%
	S-3-0.15-1.2	55	0.15	110.3	486	118.5	109.3	7.76%
	S-3-0.15-1.4	60	0.15	110.3	486	143.5	130.8	8.85%

n denotes axial compression ratio, P_{ue} and P_{uc} are the tested and computed peak loads

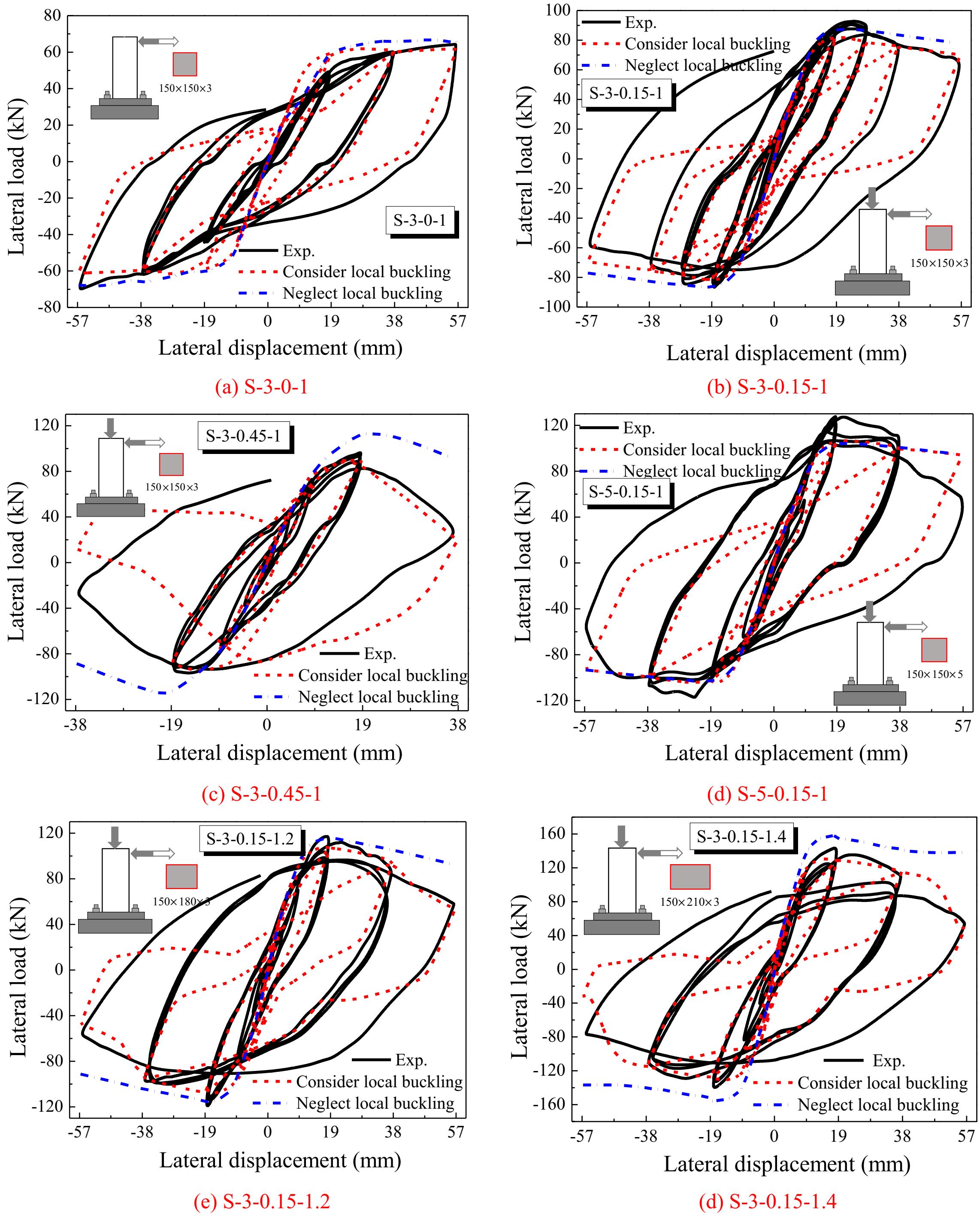

Fig. 12 The computation of P–Δ hysteretic curves (Cai 2022)

4 Proposed *N–M* Interaction Curve

In this work, 36 rectangular UHPCFST columns subjected to combined axial compression and bending were collected to assess the applicability of current code provisions. Details of the specimens are summarized in Table 5.

4.1 Assessment of Current Design Codes

Although the load-deformation curve can reveal the working mechanism and describe mechanical properties of UHPCFSTs, it is not convenient for engineering applications. Therefore, a practical calculation method is needed.

Table 5 Experimental database of rectangular UHPCFSTs under combined axial compression and bending

Source	$b \times h$ (mm)	t (mm)	L (mm)	f_c (MPa)	f_y (MPa)	ξ	N (kN)	M_t (kN·m)	M_c (kN·m)	M_c/M_t
Zhang et al. (2020)	120×120	4	600	145.9	460.3	0.467	1401	48.6	66.6	1.370
	120×120	4	600	145.9	460.3	0.467	1052	59.3	70.8	1.194
	120×120	4	1200	145.9	460.3	0.467	1212	53.5	69.6	1.301
	120×120	6	600	145.9	430.6	0.692	1752	60.1	66.5	1.106
	120×120	6	600	145.9	430.6	0.692	1317	75.2	76.5	1.017
	120×120	6	1200	145.9	430.6	0.692	1468	68.4	73.8	1.079
Yan et al. (2021b)	120×120	6	600	141.2	435.6	0.724	1054	77.1	78.5	1.018
	120×120	6	600	141.2	435.6	0.724	1035	79	78.7	0.996
	120×120	6	600	141.2	435.6	0.724	1379	74.8	74.4	0.995
	120×120	6	600	141.2	435.6	0.724	1396	78.2	74.1	0.948
	120×120	6	600	141.2	435.6	0.724	2029	54	54.8	1.015
	120×120	6	600	141.2	435.6	0.724	2000	45.7	56.1	1.228
	120×120	7.7	600	141.2	442.1	0.990	1231	87.4	88.1	1.008
	120×120	7.7	600	141.2	442.1	0.990	1255	91.6	87.7	0.957
	120×120	7.7	600	141.2	442.1	0.990	1415	82.3	85.2	1.035
	120×120	7.7	600	141.2	442.1	0.990	1619	81.6	80.8	0.990
	120×120	7.7	600	141.2	442.1	0.990	2197	52.4	61.3	1.170
	120×120	7.7	600	141.2	442.1	0.990	2215	68	60.6	0.891
Huang et al. (2020)	120×120	5	500	125.6	1030.6	1.560	2713	88.2	85.8	0.973
	120×120	5	500	125.6	1030.6	1.560	2022	131.4	110.2	0.839
	120×120	5	500	125.6	1030.6	1.560	1472	143.5	121.8	0.849
Cai (2022)	100×200	14	1000	128.1	461	2.213	1019	230	299.6	1.303
	100×200	10	950	128.1	471	1.430	896	212	237.9	1.122
	100×150	10	800	128.1	471	1.626	700	155	143.5	0.926
	100×150	10	800	128.1	471	1.626	1400	138	136.4	0.988
	100×200	18	700	128.1	426	3.511	843	190	206.6	1.087
	100×150	18	700	128.1	426	3.011	1097	292	340.3	1.165
	150×150	3	950	110.3	486	0.375	472	84.8	91.2	1.075
	150×150	4	950	110.3	430	0.452	484	97.1	95.6	0.985
	150×150	5	950	110.3	417	0.559	506	106.1	117.4	1.107
	150×150	6	950	110.3	371	0.610	507	108.6	134.6	1.239
	150×150	3	950	110.3	486	0.375	0	66.8	70.1	1.049
	150×150	3	950	110.3	486	0.375	943	112	101.6	0.907
	150×150	3	950	110.3	486	0.375	1415	92.5	101.4	1.096
	150×180	3	950	110.3	486	0.342	556	126.9	112.5	0.887
	150×210	3	950	110.3	486	0.319	641	168.6	136.3	0.808
MV										1.04

M_t and M_c are the computed and tested ultimate bending strength

At present, there are several code provisions for predicting ultimate strength of composite structures, such as AISC 360-10 (2010), EC4 (2004), GB50936 (2014) and AIJ (2001). However, these code provisions are focused on normal concrete. Considering the significant differences in mechanical properties between UHPC and normal concrete, these codes may be not appropriate for UHPCFSTs. In this work, the experimental database in Table 5 was used to assess the applicability of these code provisions. Mean values (MVs) and standard deviations (SDs) of the bending strengths of

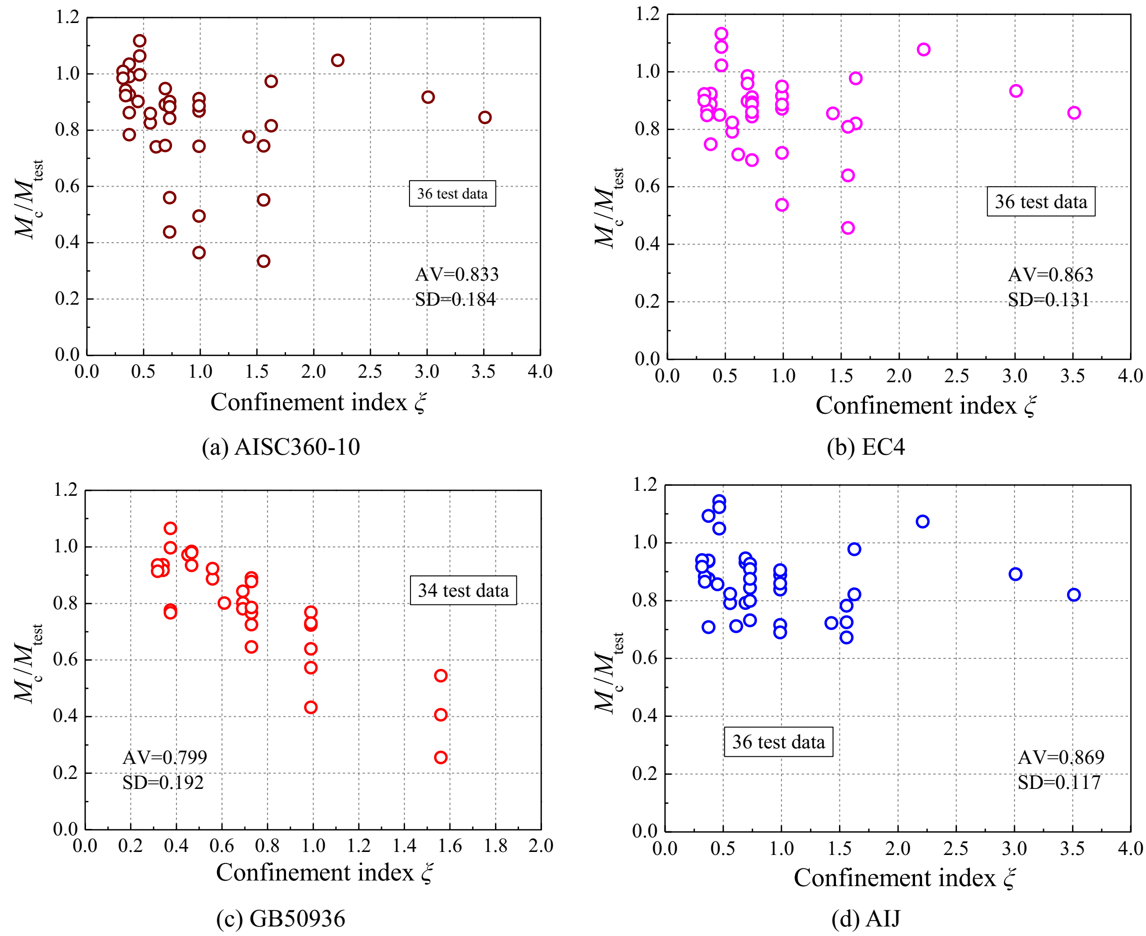

Fig. 13 The comparison of ultimate bending strength between codes and test results

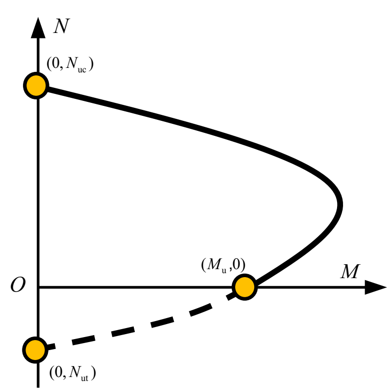

Fig. 14 A typical *N*–*M* interaction curve

the specimens were computed by design codes AISC 360-10, EC4, GB50936 and AIJ. As can be seen in the computed results shown in Fig. 13, MVs were 0.833, 0.863, 0.799 and 0.869, respectively, which suggests that all these code provisions undervalue the ultimate bending strengths of UHPCFSTs. The maximum error between computed and tested value reached 74.5% in Fig. 13c.

4.2 Proposed Practical Method

In this work, a novel and simplified *N*–*M* interaction curve of UHPCFSTs was developed, as shown in Fig. 14, and the expression is given by Eq. (7):

$$\frac{M}{M_u} = \left(1 - \frac{N}{N_{uc}}\right)\left(1 - \frac{N}{N_{ut}}\right) \tag{7}$$

where M_u denotes the pure bending strength,N_{uc} and N_{ut} denote the axial compression and tensile strengths. It can be inferred that the parabola always goes through these three points:$(0, N_{uc})$,$(0, N_{ut})$,$(M_u, 0)$.

1. Axial compression strength N_{uc}

Table 6 The experimental database of square UHPCFSTs under axial compression

Source	$b \times h$ (mm)	t (mm)	L (mm)	f_c (MPa)	f_y (MPa)	ξ	N_{ue} (kN)
Xiong et al. (2017a)	150×150	8	450	152.3	779	1.294	6536
	150×150	8	450	157.2	779	1.254	6715
	150×150	8	450	147	779	1.341	6616
	150×150	8	450	164.1	779	1.201	7276
	150×150	8	450	148	779	1.332	6974
	150×150	12	450	152.3	756	2.071	8585
	150×150	12	450	157.2	756	2.007	8452
	150×150	12	450	147	756	2.146	8687
	150×150	12	450	164.1	756	1.922	8730
	150×150	12	450	148	756	2.131	8912
	150×150	12.5	450	152.3	446	1.289	5953
	150×150	12.5	450	157.2	446	1.248	5911
	150×150	12.5	450	147	446	1.335	6039
	150×150	12.5	450	164.1	446	1.196	6409
	150×150	12.5	450	148	446	1.326	6285
Chen et al. (2018)	100×100	2	300	113.2	348.7	0.262	1406
	100×100	2	300	130.8	348.7	0.227	1575
	100×100	3.84	300	113.2	306.7	0.470	1544
	100×100	3.79	300	130.8	306.7	0.401	1676
	100×100	7.59	300	113.2	371.6	1.280	1976
	100×100	7.63	300	130.8	371.6	1.115	2051
Yan et al. (2019)	100×100	4.9	300	89.2	668.8	1.718	1800
	100×100	4.9	300	100.3	668.8	1.528	2003
	100×100	5.8	300	100.3	646.2	1.802	2220
	100×100	5.8	300	111.3	646.2	1.624	2391
	100×100	5.8	300	128.1	646.2	1.411	2573
	100×100	6.8	300	89.2	599.5	2.282	2209
	100×100	6.8	300	100.2	599.5	2.032	2294
	100×100	6.8	300	111.3	599.5	1.829	2368
	100×100	6.8	300	128.1	599.5	1.589	2492
	100×100	10	300	89.2	458.6	2.892	2206
	100×100	10	300	111.3	458.6	2.318	2298
	100×100	10	300	128.1	458.6	2.014	2498
	100×100	14.2	300	89.2	468.6	4.994	3107
	100×100	14.2	300	111.3	468.6	4.002	3120
	100×100	14.2	300	128.1	468.6	3.478	3274
	100×100	18.5	300	128.1	444.6	5.274	3441

N_{ue} is the tested axial compression strength

In this work, the experimental database of square UHPCFSTs under axial compression was established which covers a wide range of geometrical and material parameters, as shown in Table 6.

Based on the superposition theory and considering the passive confinement to the UHPC, N_{uc} was obtained by regression analysis (Fig. 15) as shown in Eq. (8):

$$N_{uc} = f_c A_c (1 + 1.11\xi) \tag{8}$$

Previous experimental research indicated that, the coefficient in Eq. (8) was about 1.5 for circle steel tube-confined ordinary concrete columns and about 1.25 for circle steel tube-confined UHPC columns. This is mainly because the dilatability of UHPC is not as prominent as that for ordinary concrete. In this work, the coefficient was smaller than 1.25 because of weaker confinement effect of rectangular steel tubes compared with that of circle steel tubes.

2. Pure bending strength M_u

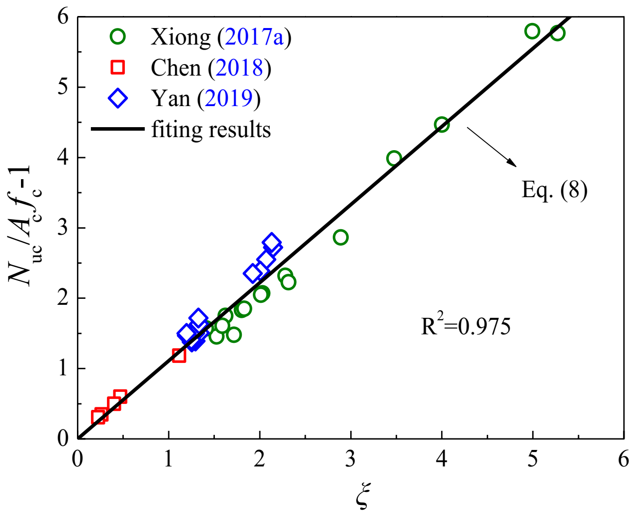

Fig. 15 The regression analysis of N_{uc}

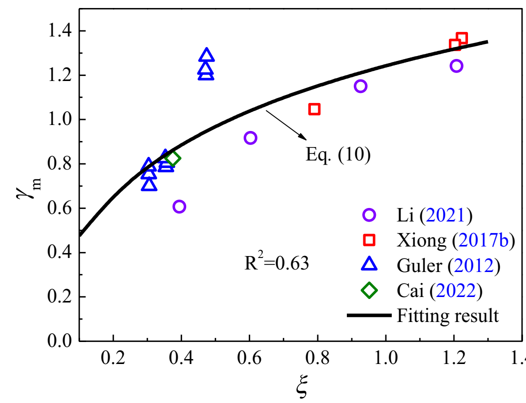

Fig. 16 The regression analysis of γ_m

An experimental database of square UHPCFST beams subjected to flexure was established, as shown in Table 7.

Based on the unified theory of CFSTs (Yu et al. 2013), M_u was calculated using the following formula:

$$M_u = \gamma_m f_{sc} W_{sc} \tag{9}$$

where $f_{sc}(f_{sc} = N_{uc}/A_{sc})$ denotes the composite strength, A_{sc} denotes the area of whole section. W_{sc} denotes flexural modulus and γ_m denotes the plastic coefficient. Referring to the research by Han (2016), γ_m was obtained by regression analysis (Fig. 16) and the expression is shown as Eq. (10):

$$\gamma_m = 1.2 + 0.45 \ln(\xi + 0.1) \tag{10}$$

3. Axial tensile strength N_{ut}

N_{ut} was calculated using the following formula (Lai et al. 2020):

$$N_{ut} = (1.1+0.4\alpha_s)A_sf_y + 0.9A_cf_t \tag{11}$$

where a_s denotes the steel content which is taken as $a_s = A_s/A_{sc}$, f_t is the tensile strength of UHPC.

In this work, the experimental database in Table 5 was used to evaluate the validity of the proposed practical

Table 7 The experimental database of square UHPCFSTs under pure bending

Source	$b \times h$ (mm)	t (mm)	L (mm)	f_c (MPa)	f_y (MPa)	ξ	M_e (kN·m)
Li et al. (2021)	150×150	4	1600	102.8	350	0.394	45.2
	150×150	4	1600	102.8	535	0.603	79.3
	150×150	6	1600	101.3	517	0.927	112.5
	150×150	6	1600	101.6	485	1.208	132.5
Xiong et al. (2017b)	200×200	12.5	2400	180	465	0.791	361
	200×200	12	2400	180	756	1.224	599
	200×200	12	2400	183	756	1.203	590
Guler et al. (2012)	80×80	2.51	1200	130.7	288	0.305	9.92
	80×80	2.51	1200	130.7	288	0.304	10.42
	80×80	2.52	1200	130.7	288	0.305	9.26
	80×80	3.02	1200	132.5	277	0.354	10.67
	80×80	3.04	1200	132.5	277	0.358	10.9
	80×80	3.01	1200	132.5	277	0.353	11.21
	80×80	4.04	1200	134.1	268	0.474	18.13
	80×80	4.03	1200	134.1	268	0.472	17
	80×80	4.02	1200	134.1	268	0.471	17.35
Cai (2022)	150×150	3	950	110.3	486	0.375	66.8

M_e is the tested pure bending strength

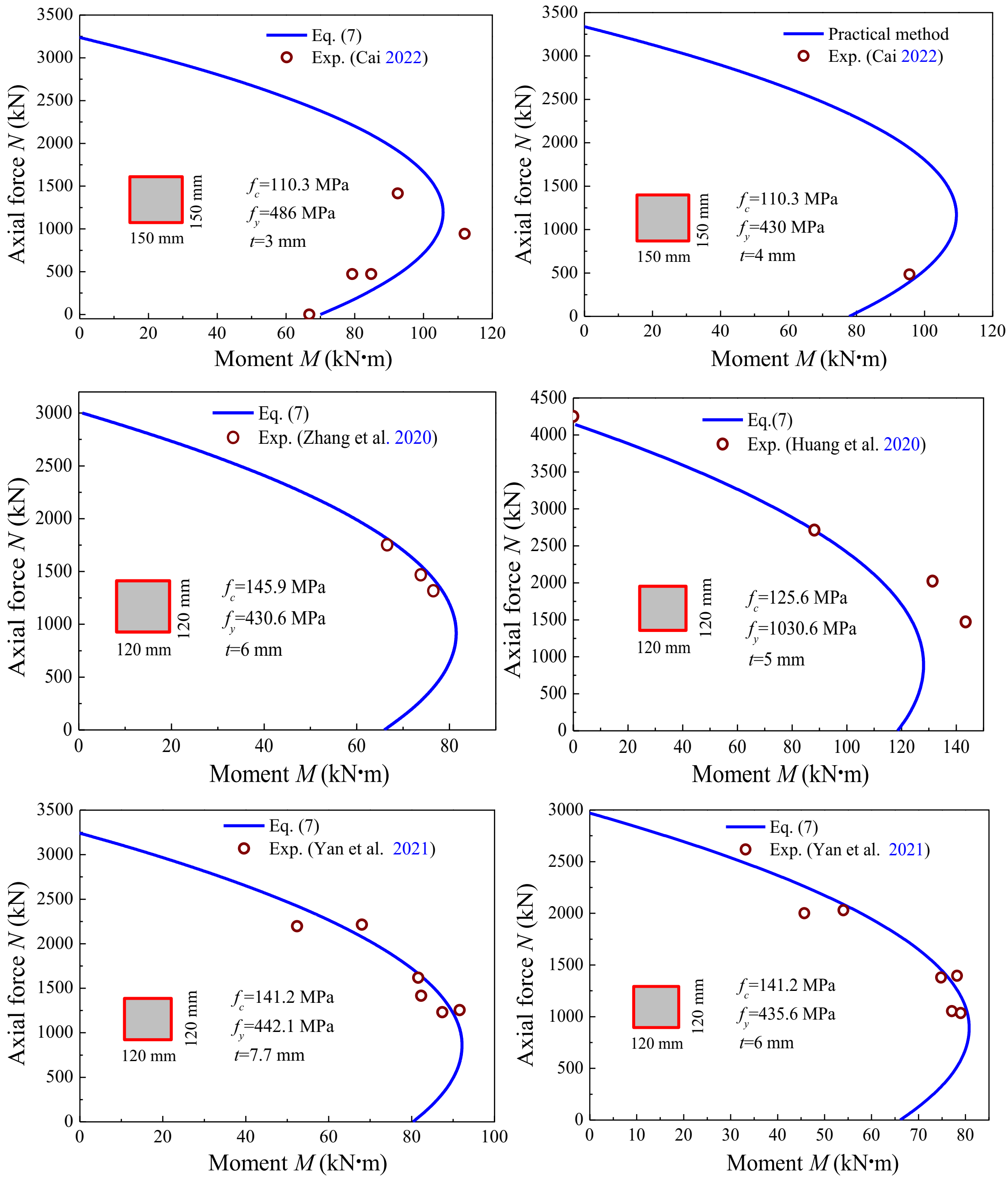

Fig. 17 The comparisons of proposed N–M interaction curves with test values

method. As can be seen in Figs. 17, 18 and Table 5, the computed results using Eq. (7) show a reasonably good agreement with the tested values. The MV of M_c/M_t is 1.04.

The discrepancy between the practical method and experimental results is related to the uncertainty of UHPC strength.

5 Conclusions

In this paper, a FBE model considering local buckling and passive confinement effect was developed to compute the nonlinear responses of UHPCFSTs. Meanwhile, an experimental database of UHPCFSTs was established and used to

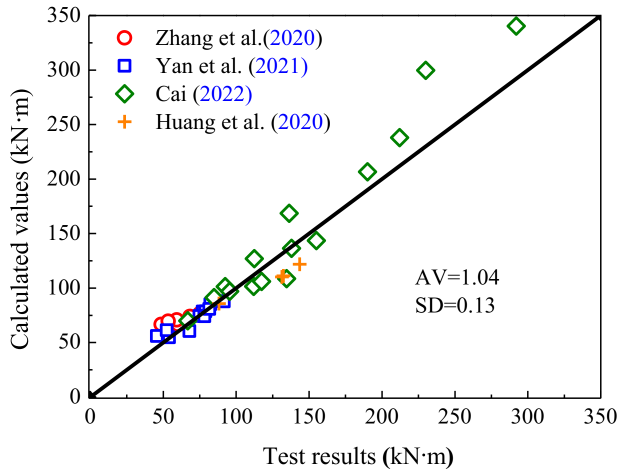

Fig. 18 The comparison of ultimate bending strengths between computed and test results

comprehensively evaluate the effects of local buckling and the suitability of current code provisions. Finally, a novel and simplified *N*–*M* interaction curve was put forward. The following conclusions can be drawn from the analysis in this work:

1. The established FBE model can accurately simulate the axial compression, eccentric compression, pure bending and cyclic behaviors of UHPCFST members.
2. Neglecting local buckling of thin-walled steel tubes would result in overestimation of the peak loads and residual strengths (post-peak ductility) of UHPCFSTs by up to 16.4%. To provide sufficient confinement to the core UHPC and reduce the effect of local buckling, the width-to-thickness ratios of rectangular steel tubes must be less than 30 in engineering design.
3. Because of significant differences in mechanical properties between UHPC and normal concrete, the current code provisions markedly undervalue the ultimate bending strength of UHPCFSTs, with a maximum error of 74.5%.
4. Based on the collected experimental database, a novel and simplified *N*–*M* interaction curve was established for predicting the ultimate bending strengths of UHPCFSTs with a high MV accuracy of 1.04.

The nonlinear responses of UHPCFSTs were computed by numerical simulation and the UHPCFST members are the main research objects. To promote the application of UHPCFSTs in engineering, the established FBE model will be used to compute nonlinear behaviors of the UHPCFST framework in future.

Acknowledgements The authors are grateful for the Key Program of National Natural Science Foundation of China (Grant No. 51738011).

References

Ahmed M, Liang QQ, Patel VI et al (2012) Nonlinear analysis of rectangular concrete-filled double steel tubular short columns incorporating local buckling. Eng Struct 175:13–26

Ahmed M, Liang QQ, Patel VI et al (2020) Nonlinear analysis of square concrete-filled double steel tubular slender columns incorporating preload effects. Eng Struct 207:110272

AIJ (2001) Recommendations for design and construction of concrete filled steel tubular structures. Architectural Institute of Japan, Tokyo

AISC360-10 (2010) Specification for structural steel buildings. American Institute of Steel Construction, Chicago

Cai H (2022) Seismic behavior and hysteretic model research on the ultra-high performance concrete filled rectangular steel tube columns. Wuhan University, Wuhan

Cai H, Deng FQ, Yan YX (2022) Nonlinear analysis on the static and cyclic behaviors of UHPC filled rectangular steel tube columns. Ksce J Civ Eng 26(3):1316–1328

Cai H, Xu LH, Chi Y (2021) Seismic performance of rectangular ultra-high performance concrete filled steel tube (UHPCFST) columns. Compos Struct 259:113242

Chen SM, Zhang R, Jia LJ (2018) Structural behavior of UHPC filled steel tube columns under axial loading. Thin Wall Struct 130:550–563

Dhakal RP, Maekawa K (2002) Path-dependent cyclic stress-strain relationship of reinforcing bar including buckling. Eng Struct 24:1383–1396

Dodd LL, Restrepo-Posada JI (1995) Model for predicting cyclic behavior of reinforcing steel. J Struct Eng ASCE 121:433–445

EC4 (2004) Design of composite steel and concrete structures. European Committee for Standardization, Brussels

GB50936-2014 (2014) Ministry of Housing and Urban-Rural Development, People's Republic of China. Technical code for concrete filled steel tubular structures. China Architecture & Building Press, Beijing

Graybeal BA (2007) Compressive behavior of ultra-high-performance fiber-reinforced concrete. ACI Mater J 104(2):146–152

Guler S, Copur A, Aydogan M (2012) Flexural behavior of square UHPC-filled hollow steel section beams. Struct Eng Mech 43(2):225–237

Habel K, Viviani M, Denarié E et al (2006) Development of the mechanical properties of an ultra-high performance fiber reinforced concrete(UHPFRC). Cem Concr Res 36(7):1362–1370

Han LH (2016) Concrete filled steel tubular structures: from theory to practices. Science Press, Beijing

Hannawi K, Bian H, Prince-Agbodjan W et al (2016) Effect of different types of fibers on the microstructure and the mechanical behavior of ultra-high performance fiber-reinforced concretes. Compos B Eng 86:214–220

Hassan AMT, Jones SW, Mahmud GH (2012) Experimental test methods to determine the uniaxial tensile and compressive behaviour of ultra high performance fibre reinforced concrete (UHPFRC). Constr Build Mater 37:874–882

Hu AX, Liang XW, Yu J (2018) Experimental study of uniaxial tensile characteristics of ultra-high performance concrete. J Hunan Univ 45(9):30–37

Huang ZC, Uy B, Li DX et al (2020) Behavior and design of ultra-high-strength CFST members subjected to compression and bending. J Constr Steel Res 175:106351

Jiang YD, Silva A, Macedo L et al (2019) Concentrated-plasticity modelling of circular concrete-filled steel tubular members under flexure. Structures 21:156–166

Kabir H, Aghdam MM (2019) A robust Bézier based solution for nonlinear vibration and post-buckling of random checkerboard graphene nano-platelets reinforced composite beams. Compos Struct 212:184–198

Kamila GM, Liang QQ, Hadi MNS (2019) Fiber element simulation of interaction behavior of local and global buckling in axially loaded rectangular concrete-filled steel tubular slender columns under fire exposure. Thin Wall Struct 145:106403

Lai ZC, Varma AH (2016) Effective stress-strain relationships for analysis of noncompact and slender filled composite (CFT) members. Eng Struct 124:457–472

Lai ZC, Varma AH, Griffis LG (2016) Analysis and design of noncompact and slender CFT beam-columns. J Struct Eng 142(1):04015097

Lai ZC, Yao PY, Huang WJ (2020) Reactive powder concrete-filled steel tube (RPCFT) members subjected to axial tension: experimental study and design. Structures 28:933–942

Le HA, Fehling E (2017) Assessment of stress-strain model for UHPC confined by steel tube stub columns. Struct Eng Mech 63:371–384

Le HA, Fehling E, Thai DK (2018) Simplified stress-strain model for circular steel tube confined UHPC and UHPFRC columns. Steel Compos Struct 29(1):125–138

Li JY, Deng ZC, Sun T (2021) Flexural behavior of ultra-high performance concrete filled high-strength steel tube. Struct Concrete 22(3):1688–1707

Liang QQ, Uy B, Liew JYR (2007) Local buckling of steel plates in concrete filled thin-walled steel tubular beam-columns. J Constr Steel Res 63:396–405

Mander JB, Priestly MNJ, Park R (1988) Theoretical stress–strain model for confined concrete. J Struct Eng 114:1804–1826

Ren GM, Wu H, Fang Q et al (2017) Tri-axial compressive behavior of UHPC and applications in the projectile impact analyses. J Constr Steel Res 136:238–255

Sakino K, Nakahara H, Morino S (2004) Behavior of centrally loaded concrete-filled steel-tube short columns. J Struct Eng 130(2):180–188

Tao Z, Katwal U, Uy B et al (2021) Simplified nonlinear simulation of rectangular concrete-filled steel tubular columns. J Struct Eng 147(6):04021061

Uy B (2000) Strength of concrete filled steel box columns incorporating local buckling. J Struct Eng 126:341–352

Valipour HR, Foster SJ (2010) Nonlinear static and cyclic analysis of concrete-filled steel columns. J Constr Steel Res 66:793–802

Vrcelj Z, Uy B (2002) Strength of slender concrete-filled steel box columns incorporating local buckling. J Constr Steel Res 58:275–300

Xiong MX, Xiong DL, Liew JYR (2017a) Axial performance of short concrete filled steel tubes with high-and ultra-high-strength materials. Eng Struct 136:494–510

Xiong MX, Xiong DL, Richard LJY (2017b) Flexural performance of concrete filled tubes with high tensile steel and ultra-high strength concrete. J Constr Steel Res 132:191–202

Xu LH, Wu FH, Chi Y et al (2019a) Effects of coarse aggregate and steel fibre contents on mechanical properties of high performance concrete. Constr Build Mater 206:97–110

Xu LH, Lu QR, Chi Y et al (2019b) Axial compressive performance of UHPC filled steel tube stub columns containing steel-polypropylene hybrid fiber. Constr Build Mater 204:754–767

Yan YX, Xu LH, Li B et al (2019) Axial behavior of ultra-high performance concrete (UHPC) filled stocky steel tubes with square sections. J Constr Steel Res 158:417–428

Yan JB, Chen AZ, Zhu JS (2021a) Behaviours of square UHPFRC-filled steel tubular stub columns under eccentric compression. Thin Wall Struct 159:107222

Yan Y, Liu B, Xing Y et al (2021b) Free vibration analysis of variable stiffness composite laminated beams and plates by novel hierarchical differential quadrature finite elements. Compos Struct 274:114364

Yu M, Zha XX, Ye JQ (2013) A unified formulation for circle and polygon concrete-filled steel tube columns under axial compression. Eng Struct 49:1–10

Zhang R, Chen SM, Gu P (2020) Structural behavior of UHPC filled steel tubular columns under eccentric loading. Thin Wall Struct 156:106959

Zohrevand P, Mirmiran A (2011) Behavior of ultra high performance concrete confined by fiber reinforced polymers. J Mater Civil Eng 23(12):1727–1734